ADVANCED MATERIALS FOR ADDITIVE MANUFACTURING

Microstructure and Mechanical Properties of an Advanced Ag-Microalloyed Aluminum Crossover Alloy Tailored for Wire-Arc Directed Energy Deposition

THOMAS KLEIN,[1,5] AUREL ARNOLDT,[1] MANUEL GOMES,[2] and PERE BARRIOBERO-VILA[3,4]

1.—LKR Light Metals Technologies Ranshofen, Austrian Institute of Technology, 5282 Ranshofen, Austria. 2.—Instituto de Soldadura e Qualidade, 2740-120 Porto Salvo, Portugal. 3.—German Aerospace Center (DLR), Institute of Materials Research, 51147 Cologne, Germany. 4.—Department of Materials Science and Engineering, Technical University of Catalonia (UPC), Eduard Maristany Av. 16, 08019 Barcelona, Spain. 5.—e-mail: thomas.klein@ait.ac.at

The implementation of wire-arc directed energy deposition requires the development of novel, process-adapted, high-performance aluminum alloys. Conventional high-strength alloys are, however, difficult to process as they are prone to hot-cracking. Crossover alloys based on Al-Mg-Zn combine good processability with good mechanical properties following artificial aging. Here, we present an effort to further improve the mechanical properties of Al-Mg-Zn crossover alloys using Ag microalloying. No cracks and few porosities were observed in the samples. The microstructure is dominated by fine and globular grains with a grain size ≈ 26.6 μm. The grain structure is essentially free of texture and contains fine microsegregation zones with $\approx$ 3–5 μm thickness of segregation seams. Upon heat treatment these microsegregation zones are dissolved and T-phase precipitates are formed as clarified by diffraction experiments. This precipitation reaction results in a microhardness of $\approx$ 155 HV0.1, a yield strength of 391.3 MPa and 418.6 MPa, an ultimate tensile strength of 452.7 MPa and 529.4 MPa and a fracture strain of 3.4% and 4.4% in transversal and in longitudinal directions, respectively. The gained results suggest that highly loaded structures can be manufactured by wire-arc directed energy deposition using the newly developed aluminum crossover alloy.

INTRODUCTION

The ever-increasing demands on structural components with new functionalities used, for example, in aerospace industries, require the development of novel, process-specific metal materials. With the advent of additive manufacturing (AM), alloys are needed that show robust processability in addition to good mechanical performance.[1,2] High-strength aluminum alloys such as 2xxx[3] or 7xxx[4] series are, however, challenging to process via AM. These challenges mostly arise from their high hot-cracking susceptibility.[5]

Wire arc directed energy deposition (waDED) uses metal feedstock wires, which are melted by an energy source such as an electric or plasma arc.[6,7] The droplet formed on the wire tip is then deposited according to a predefined path.[8] waDED is particularly suitable for large structures with medium complexities.[9] Together with high-performance aluminum alloys, the technology is envisaged to be used in future structural applications in aviation industry including fabrication of fuselage or wing structures,[10] whereby conventional manufacturing and AM could be combined in hybrid manufacturing in a highly flexible manner.[11]

As feedstock material, commercially available welding wires are mostly used.[7] The processing behavior and resultant properties of aluminum feedstock wires have

recently been summarized in Ref. [12]. However, very few high-performance alloy wires are available on the market, mainly due to their challenging behavior during fusion welding.[13] Recently it has been demonstrated that modest adaptions of the alloy composition of 6xxx[14] and 7xxx[15] can result in improved processing behavior while maintaining the excellent mechanical properties of high-strength aluminum alloys. A different yet promising strategy is the incorporation of nano-particles into high-strength aluminum alloys.[16] However, the processing windows to fabricate intricate structures with sufficient structural integrity remains narrow.

Crossover alloys based on the Al-Mg-Zn-Cu system can offer a more robust processing window for waDED with mechanical properties comparable to high-strength 2xxx and 7xxx alloys.[17] It was shown that the increased Mg/Zn ratio results in drastically reduced hot-cracking susceptibility and enables excellent control over precipitation reactions.[18] Through the increased Mg/Zn ratio the precipitate structure changes from η-phase to T-phase.[19] The combination of technological and mechanical properties makes these alloys suitable candidates for future large-scale additive manufactured components with robust processability and high load-bearing capacity. More details on crossover alloys can be found in a recent review from Stemper et al.[20]

This study aims at characterizing a novel high-performance alloy for use in waDED for fabrication of highly loaded structures. For this purpose, focus is on the effects of microalloying Ag to an Al-5.4 Mg-3.8Zn-0.3Cu (wt.%) base alloy and its effects on the property improvement after waDED processing and ensuing heat treatment. Significant enhancement of mechanical performance was reported for similar alloys processed via casting, subsequent forming operations and heat treatments.[21] In crossover alloys[22] as well as in conventional 7xxx alloys,[23] Ag has been shown to have a beneficial effect on peak strength properties. However, the complex interactions with unique AM specific processing conditions have not been studied so far. For this purpose, feedstock wires were custom made and processed by waDED. After subsequent heat treatment the samples were characterized using scanning electron microscopy (SEM) and electron back-scatter diffraction (EBSD) as well as high-energy synchrotron X-ray diffraction (HEXRD). The mechanical properties were assessed using hardness profiles and tensile testing. Concomitantly, the evolution of phases was calculated using thermodynamic simulations. The gained results address the need for novel and advanced alloys dedicated for waDED and contribute to the understanding of microalloying effects on the behavior of additively manufactured crossover alloys.

MATERIALS, PROCESSING AND METHODOLOGIES

Chemical Composition and Processing Conditions

The feedstock wires were manufactured using vertical continuous casting with a hot top die.

Etched slices did not show any porosities, which would, moreover, be closed by the subsequent wire fabrication route. From the slab, billets were machined after a stress relief heat treatment. After heating the billets in a chamber furnace, these were continuously extruded to wires with 1.6 mm diameter. The complete wire fabrication route is schematically shown as a flow chart in Fig. 1.

The chemical composition was determined by optical emission spectroscopy with a SPECTRO-MAXx 6 from SPECTRO Analytical Instruments GmbH. The chemical analysis was conducted according to OENORM EN 14.726. Values were determined by averaging over at least three individual measurements.

Specimen fabrication was performed using the waDED parameters given in Table I with a Cold Metal Transfer (CMT) AC welding characteristic in combination with an ABB IRB 4600 robot and a tilting rotary table. This process has been shown to be well suited for waDED of aluminum structures because of its low heat input.[24,25] The droplet transition sequence during CMT has been recently analyzed in detail in Ref. [26]. The deposition rate (DR) given in Table I in kg/h was estimated according to Eq. 1:

$$DR = 60 \cdot \rho \cdot \overline{v}_{WF} \cdot A_{WW} \qquad (1)$$

where ρ is the material density in kg/m^3, v_{WF} is the mean wire feed speed in m/min, and A_{ww} is the welding wire cross-sectional area in m^2. The density of the investigated alloy is approximately 2.77×10^3 kg/m^3 and wire cross-section area is 2.01×10^{-6} m^2 (Ø 1.6 mm). The parameter set applied was adjusted based on a preliminary parameter study alongside with cross-sectional analysis and visual inspection. The fewest porosities and absence of cracks were achieved with the parameter set summarized in Table I. The dimensions of the fabricated samples were 120 mm × 130 mm × 5 mm consisting of 76 layers with an exemplary photograph shown in Fig. 2a. An AA6082 sheet with 2 mm thickness was used as substrate. The mean roughness of the structure is approximately 0.3 mm, and no periodic disturbances, i.e., humping phenomenon, were observed in the samples investigated. Further information on the humping phenomenon can be found in Ref. [27].

An artificial age-hardening treatment was performed as schematically visualized in Fig. 2b consisting of a solution heat treatment (SHT) stage and a two-step artificial aging (AA) treatment. The SHT was performed in a Nabertherm N120/85HA chamber furnace at 470°C for 40 min followed by rapid immersion in water. The AA was conducted in a Heraeus UT 6200 heating oven at 100°C for 3 h followed by 175°C for 9 h and cooling in air. These parameters were chosen based on the work of Stemper et al.,[22] who showed that reasonable aging

Microstructure and Mechanical Properties of an Advanced Ag-Microalloyed Aluminum
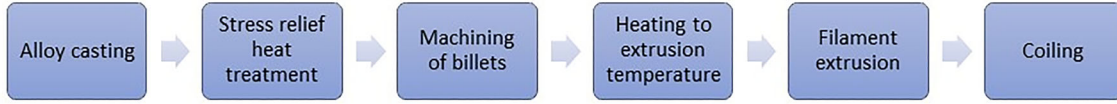Crossover Alloy Tailored for Wire-Arc Directed Energy Deposition

Fig. 1. Flow chart of the wire fabrication route.

times without significant strength trade-off can be achieved using this three-staged scheme.

Computational and Experimental Methods

Thermodynamic Calculations

The stability and fractions of stable phases of the present alloy composition were calculated using Thermo-Calc 2021b with the TTAl8 thermodynamic database. Additionally, Scheil-Gulliver simulations were used to estimate non-equilibrium conditions prevailing during waDED. Potential solute trapping effects occurring because of the rapid cooling sequence were accounted for in this model, whereby cooling rates were estimated based on published results.[28] The information from thermodynamic simulations was further utilized to establish the optimum SHT temperature.

Microstructure Characterization Techniques

SEM was conducted using a Tescan Mira 3 at 20 kV acceleration voltage in back-scattered electron (BSE) mode. Metallographic specimens were manufactured using successively finer abrasive paper grades followed by mechano-chemical polishing with colloidal silica. The secondary electron (SE) mode was used to analyze fracture surfaces after tensile testing. EBSD was conducted using the EDAX Hikari Plus EBSD camera system together with the EDAX OIM 8 software. For clean-up, grain dilation with a tolerance of 5° and a minimum grain size of 5 pixels was used. A neighbor confidence index correlation with a minimum confidence index of 0.1 was applied.

Phase identification based on crystallographic structural information was performed using high-energy X-ray diffraction (HEXRD) performed at P07 HEMS beamline operated by Helmholtz Zentrum Hereon at Petra III at Deutsches Elektronen-Synchrotron (DESY) in Hamburg. The 2D diffraction rings were captured using a Perkin-Elmer X-ray area detector 1621 (sample-detector distance = 1537 mm). The experimental setup was calibrated using a LaB_6 sample. For analysis, the 2D patterns were azimuthally integrated using the Fit2D software. The mean energy of the synchrotron radiation was 100 keV, and the beam size was adjusted to 1×1 mm^2. Cylindrical specimens fabricated from the waDED samples with and without the heat treatment with 4 mm diameter and 8 mm length were used for the analysis using transmission-mode setup.

Table I. waDED deposition parameters used for fabrication of the waDED sample

Designation	waDED deposition parameters
Shielding gas	Argon 5.0 (Messer Austria GmbH)
Mean wire feed rate, $\overline{v}_{WF}$, [m/min]	3.5
Deposition rate, DR, [kg/h]	1.17
Current $\overline{I}$ / I_{max} [A]	84 / 97
Mean voltage $\overline{U}$ [V]	11.2
Travel speed [mm/s]	12
Energy input per unit length [J/mm]	83

Mechanical Property Characterization Techniques

Hardness values were determined using a DuraScan 70 G5 microhardness tester from ZwickRoell GmbH & Co KG with a 100 g load. The dwell time for each indent was 10 s. A line profile was determined with 0.5 mm distance between individual indents.

Tensile testing was conducted using two different facilities: (1) an Instron 8800 universal testing machine equipped with a 30 kN load cell, whereby strains were determined using digital image correlation with two JAI 500 CCD cameras; (2) a ZwickRoell Z100 universal testing machine used in combination with contact extensometers. Gained results are considered comparable; thus, the reported values correspond to mean values of at least three individual measurements of each condition.

RESULTS AND DISCUSSION

Processing-Related Variations in Chemical Composition

The chemical compositions of the wire prior to waDED as well as of the waDED deposit are given in Table II. All values are given in mass percent. In the wire, six individual measurements provided evidence that the Ag concentration ranges from 0.20 wt.% to 0.23 wt.%. Upon waDED further homogenization is observed as all determined values were equivalent. In case of both volatile chemical elements, variations are observed; 0.4 wt.% Mg and 0.5 wt.% Zn are evaporated during the CMT deposition procedure. This is due to their high vapor pressure and affinity to even small traces of oxygen. Concentrations of Cu, Ag and Fe remain similar within the

accuracy of the compositional analysis, and no evaporation of these elements occurs. These findings are in agreement with Ref. 17.

Thermodynamic Simulations and Assessment of the Hot-Cracking Susceptibility

The phase fractions of the alloy with the actual chemical composition after deposition were calculated using thermodynamic calculations as depicted in Fig. 3. Figure 3a shows the calculation results for equilibrium conditions. Primary solidification occurs through the α-Al phase starting at approximately 620°C followed by the formation of very low fractions of intermetallic Al_3Fe phase. The onset of formation of the T-phase, which is the major hardening phase in this alloy system,[18,21] occurs at approximately 430°C with a steeply rising phase fraction below this temperature. Therefore, the SHT was set to 470°C ensuring the complete dissolution of T-phase and the possibility of its controlled re-precipitation during the ensuing AA steps at 100°C and 175°C, respectively.

A similar picture results from using the Scheil–Gulliver approach (Fig. 3b) with the complete solidification dragged to lower temperatures. Additionally, a small fraction of Al_3Mg_2 phase is predicted to form during the last stages of solidification. These data were used to assess the hot-cracking susceptibility of the alloy based on the models of Kou[29] and Liu and Kou[30] via the calculation of the hot-cracking susceptibility index (CSI) according to Eq. 2:

$$CSI = \left(\frac{\Delta T}{\Delta f_s^{(1/2)}} \right)_{max}, \qquad (2)$$

with T corresponding to the temperature and f_s to the solid phase fraction. The CSI values, hence, are the maximum slope of the tangent to the ΔT versus $\Delta f_s^{1/2}$ curve. This value amounts to 1830°C, which suggests that the alloy is more robust against hot-cracking than, for example, the AA7075[15] or AA2024[11] alloy.

Comparative Analysis of Microstructure and Hardness in As-built and Heat-treated Conditions

The microstructures of the Al-5.4 Mg-3.8Zn-0.3Cu-0.2Ag alloy in as-built and heat-treated material conditions as visualized by SEM are shown in Fig. 4. As no variations with specimen height or orientation were observed on this scale, only images taken in longitudinal direction are represented. Figure 4a shows fine-scaled microsegregation zones resulting from the rapid cooling during solidification. Characteristic dimensions of these zones are in the range of ≈ 3–5 μm and result from the pile-up of solutes ahead of the solidification front. Slight porosities with a mean diameter of ≈ 5 μm are discernible. Their predominantly globular shape
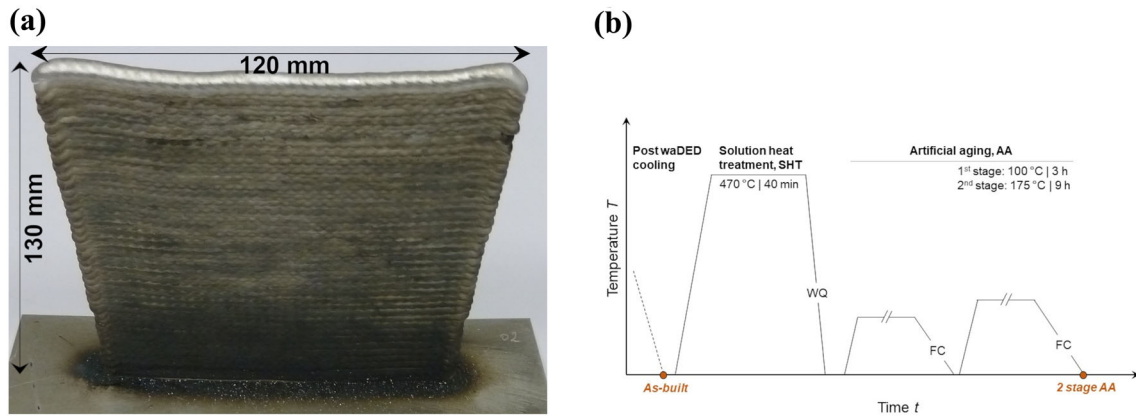

Fig. 2. (a) Photograph of an exemplary waDED sample. (b) Scheme of the post-waDED-processing heat treatment performed in the present work consisting of a SHT and two consecutive AA heat treatments.

Table II. Chemical composition of the feedstock wire and the waDED deposit. Burn-off of Mg and Zn is observed

	Al [wt.%]	Mg [wt.%]	Zn [wt.%]	Cu [wt.%]	Ag [wt.%]	Fe [wt.%]
Wire	Bal.	5.41	3.81	0.33	0.21	0.16
waDED deposit	Bal.	5.03	3.30	0.30	0.19	0.14

Microstructure and Mechanical Properties of an Advanced Ag-Microalloyed Aluminum
Crossover Alloy Tailored for Wire-Arc Directed Energy Deposition
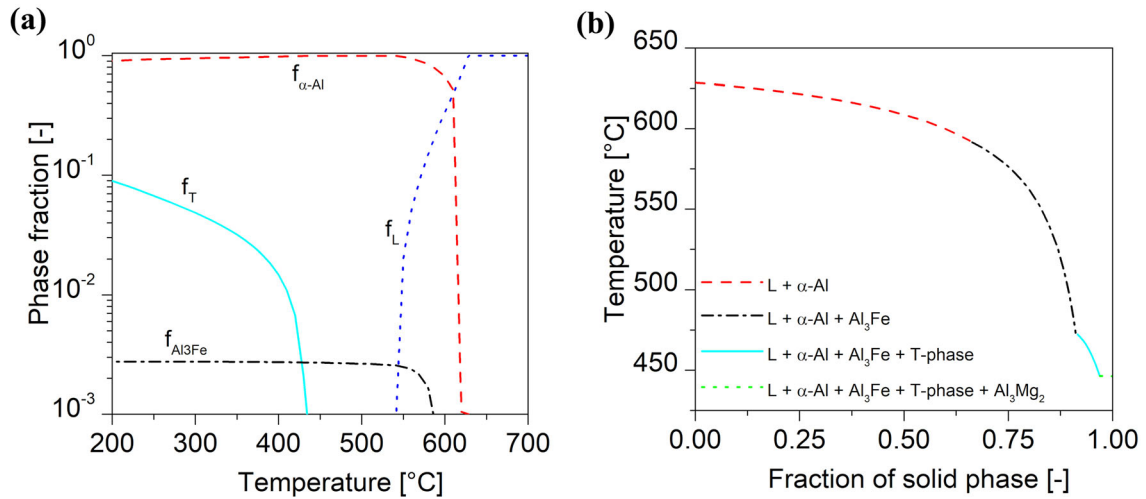

Fig. 3. Equilibrium phase fraction diagram (a) and Scheil-Gulliver simulation (b) of the Al-5.4 Mg-3.8Zn-0.3Cu-0.2Ag alloy.
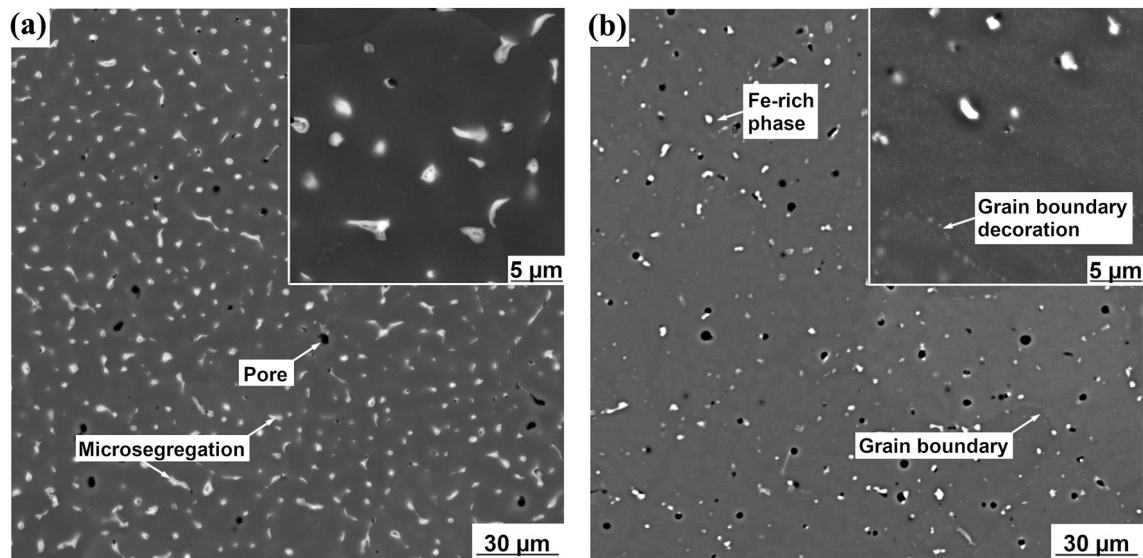

Fig. 4. SEM micrographs of the (a) as-built and (b) heat-treated material conditions. In (a) many fine microsegregations are visible with only a few pores. These microsegregations have dissolved during the SHT as visible in (b), where only Fe-rich phases remain. In the inset reprecipitated phases along grain boundaries are discernible.

suggests their nature to be gas porosities rather than shrinkage cavities, which favorably form elongated shapes remanent of the interdendritic regions.[31,32] In both material conditions Fe-rich phases with a bright contrast were observed, which are common in aluminum alloys containing traces of Fe.[33]

Upon SHT the microsegregation zones dissolve and are no longer visible in Fig. 4b. During the AA treatment, fine-scaled hardening precipitates are formed, which are too fine to be resolved by SEM. Along grain boundaries these precipitates form in a coarser manner as a grain boundary decoration as visible from the inset in Fig. 4b. In the vicinity of grain boundaries' increased diffusivity, local

segregation effects of Mg and Zn[34] as well as a reduced nucleation barrier may contribute to these coarser precipitate structures.

Results of HEXRD experiments are summarized in Fig. 5, comparing the as-built and the heat-treated material conditions. The major peaks of the α-Al phase have been indexed in this figure, which appear equivalent in both material conditions. Additional diffraction peaks that can be linked to the occurrence of the T-phase were identified in the as-built material (marked with * in Fig. 5). This phase is the dominant precipitate phase in Al-Mg-Zn alloys with a high Mg/Zn ratio,[18] whereas in alloys with a low Mg/Zn ratio the η-phase is dominant. No signal of the Al_3Mg_2 phase, which
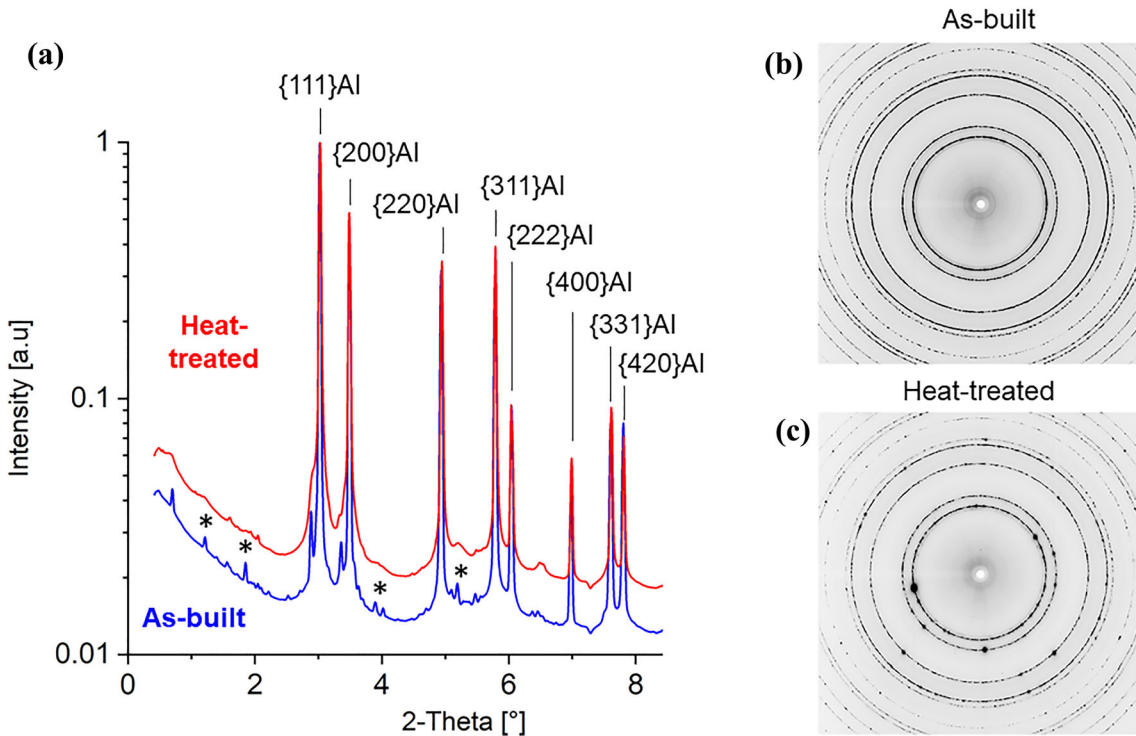
(a)

(b) As-built

(c) Heat-treated

Fig. 5. HEXRD diffractograms (a) evaluated by integration of the HEXRD images (b) and (c). In both material conditions the majority phase is α-Al. In the as-built material also image peaks belonging to the T-phase are identified and indicated by *. In the corresponding angular range broad peaks and shoulders are observed in the heat-treated material. The 2D images (b) show defined rings in the as-built condition and spotted rings in the heat-treated condition suggesting grain coarsening during the SHT.

was predicted by the Scheil-Gulliver approach, was observed, suggesting that this phase either does not form during the actual cooling rates or its amount is below the resolution limit of the HEXRD. In the heat-treated condition, shoulders and weak/broad peaks are visible at angular positions close to the T-phase, suggesting that during the SHT, coarse T-phases are dissolved, and fine particles are re-precipitated during the AA. This results in the desired hardening response. Moreover, the spottier Debye–Scherrer rings observed in Fig. 5c compared to those in Fig. 5b indicate that coarsening of the grain structure takes place during the heat treatment.

Grain Structure and Preferential Orientations

The grain structure of the heat-treated alloy is visualized by EBSD in Fig. 6, taken in longitudinal direction. The grains appear equiaxed with no favored growth of elongated structures. The mean equivalent circle diameter is ≈ 26.6 μm with locally much finer grains inferred to correspond to the fusion zones. This grain size is equivalent to previous reports of similarly processed aluminum alloys.[14] In the regions with finer grains, faster solidification occurs resulting in grain refinement.
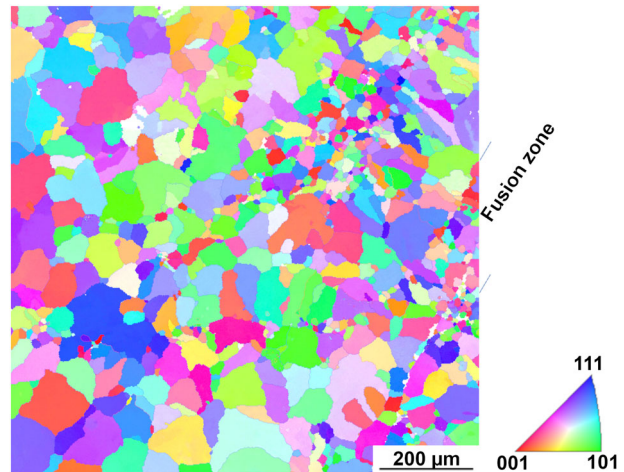

Fig. 6. EBSD IPF map of the heat-treated material condition. The grain structure does not show favored orientations, i.e., no texture. In the fusion zone (marked exemplarily) the grain structure is finer because of more rapid solidification.

The inverse pole figure (IPF) map suggests no substantially favored crystal orientations similarly to what has been reported in Ref. 14, for example, for a structurally refined AA6063 alloy (processed by CMT) but contradicting findings of Ref. 35 for an AA7055 alloy (processed by gas tungsten arc
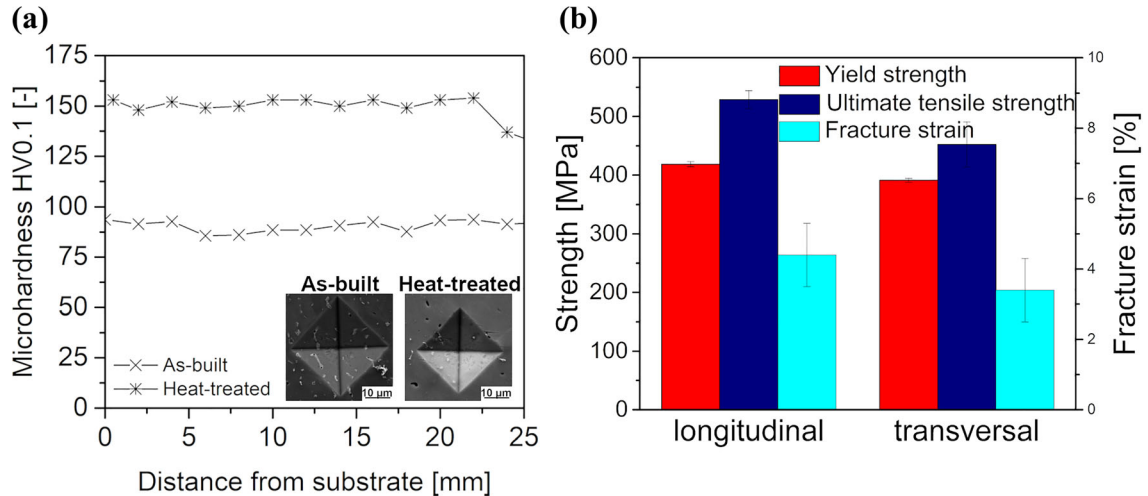
Fig. 7. (a) Hardness profiles along the as-built and heat-treated specimens' height in its lower portion. The hardness values are homogeneous and raised from approximately 95 HV to approximately 155 HV because of the AA. For comparison the microhardness indents are depicted as insets. (b) Characteristic mechanical properties of the heat-treated material condition from tensile testing with respect to specimen direction.

welding). The grain morphology results from a complex interplay of the thermal gradient, solidification rate and preferential nucleation sites, whereby the latter is strongly affected by the presence of segregating elements resulting in constitutional supercooling as rationalized by the interdependence theory.[36,37] Results of the present work and its comparison to Ref. 35, where similar alloying elements are present (although in different concentrations), suggest that the processing conditions (i.e., CMT) affect the grain structure formation to a large extent.

Mechanical Property Analysis

Hardness Profiles

An initial assessment of the effects of the heat treatment on the mechanical response of the Al-5.4 Mg-3.8Zn-0.3Cu-0.2Ag alloy was performed by hardness profile measurements. These results are shown in Fig. 7a, where only the lowest 25 mm are shown as the vicinity of the substrate is most susceptible to inhomogeneous mechanical properties because of the varying cooling conditions. Substantial hardening from $\approx$ 95 HV0.1 to $\approx$ 155 HV0.1 resulting from the heat treatment is visible. Little scattering of the data is observed in both conditions in agreement with the homogeneous microstructure observed by SEM. The hardness values of both material conditions are close to that of conventional AA7075 after waDED and heat treatment[15] and close to values of heat-treated sheet material.[38] The hardness of alloys of similar composition as used in the present work processed by different routes are of equivalent magnitude as reported in Ref. 22. In Fig. 7a two representative

microhardness indents of the two investigated material conditions are depicted. Signs of plastic deformation are visible, and no cracking is observed.

Tensile Testing

The mechanical properties of the novel Al-5.4 Mg-3.8Zn-0.3Cu-0.2Ag alloy processed by waDED and subsequently heat-treated were analyzed by tensile testing. Characteristic results are summarized in Fig. 7b. The yield strength in the range of 390–420 MPa depending on the specimen orientation is in the region of high-strength aluminum alloys outperforming materials properties reported for a similar but Ag-free alloy.[17] The yield strength, however, remains below values of heat-treated sheet metal,[38] which may be due to varying grain structure and dislocation densities. In Ref. 22 this increased hardening response, observed in the Ag-containing crossover alloy, was argued to result from strong Ag-vacancy interactions that result in a larger number of nucleation sites and thus refinement of the precipitate structure.

The anisotropy of the waDED deposited samples was addressed by calculation of the index of anisotropy, which is defined as the quotient of each property in longitudinal direction and in transversal direction rounded to one decimal place. These calculations yield values of 1.1 for the yield strength, 1.2 for the ultimate tensile strength and 1.3 for the fracture strain. The anisotropic behavior is, thus, most pronounced in ultimate tensile strength and fracture strain. This phenomenon has been linked to the presence of pores in waDED aluminum alloys.[39] Thereby, pores occur non-randomly aligned within the fusion zone because of buoyancy effects resulting in preferential alignment
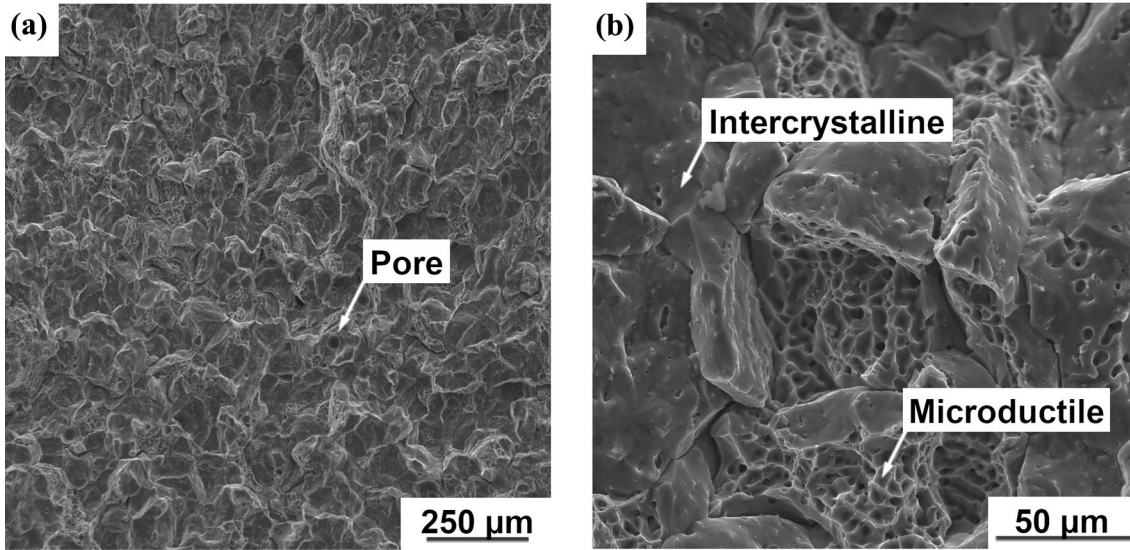
Fig. 8. Exemplary fracture surfaces in longitudinal direction in different magnifications (a, b) with indicated visible porosity. (b) Equal numbers of microductile and intercrystalline features are observed in the fracture plane.

along melt pool boundaries. Upon tension perpendicular to this plane, cracks form yielding coalescence of the aligned porosity and premature failure.[17] Further optimization and adaption of processing conditions may enable a reduction of these pores, which will result in more isotropic plastic deformation behavior.

Fracture Surface Analysis

The fracture surfaces of the tensile specimens are shown in Fig. 7a and b at different magnifications. No differences with respect to specimen direction were observed. Few pores are visible on the fracture surfaces with one marked in Fig. 8a. Their generally globular morphology suggests their identity to be gas porosities,[40] whereas an aspect ratio differing significantly from one would suggest cavities resulting from shrinkage during solidification.[32] The detailed view shown in Fig. 8b shows that mixed-mode fracture, consisting of microductile regions and intercrystalline regions randomly distributed in the fracture plane, occurs. Such mixed-mode fracture characteristics were already described in the literature to prevail in an Ag-modified hot-rolled and heat-treated AA7075 alloy.[23] It is suggested that the precipitate features present close to grain boundaries (see Fig. 4b), which are comparably coarse, reduce grain boundary cohesion. During the AA treatment these precipitates can further coarsen because of increased diffusion along grain boundaries.[28] Increasing the SHT time may provide a more homogeneous situation prior to AA or reducing the aging duration may result in fewer accumulations at the grain boundaries—both might contribute to resolving this issue.

CONCLUSION

Wire-arc directed energy deposition of an Ag-microalloyed aluminum crossover alloy (Al-5.4 Mg-3.8Zn-0.3Cu-0.2Ag) was performed. The deposited and heat-treated samples were characterized in terms of microstructure and mechanical properties. The aim of the chemical composition modification was an increase in strength, while maintaining robust processability. The following major conclusions can be drawn:

- Specimens fabricated by CMT were free of cracks. Porosities visible on the metallographic cross-sections and fracture surfaces were of globular morphology suggesting gases to be their route cause.
- Upon solidification, small-scaled microsegregation zones ($\approx$ 3–5 μm) are formed that are dissolved during the solution heat treatment. Fine-scaled T-phase precipitates are formed during artificial aging. The microstructure consists of equiaxed grains with a grain size $\approx$ 26.6 μm after the heat treatment.
- During the heat treatment conducted pronounced age hardening is observed, whereby the microhardness reaches $\approx$ 155 HV0.1 from initial $\approx$ 95 HV0.1.
- In the heat-treated state, a yield strength > 390 MPa, ultimate tensile strength > 450 MPa and fracture strain > 3% were reached, whereby the present anisotropy of the mechanical properties was explained by the presence of aligned porosities within the fusion zone.
- The fracture surfaces showed mixed-mode characteristics consisting of microductile and inter-

crystalline features, which was linked to the potential presence of a grain boundary decoration.

In summary, the investigated Ag-microalloyed aluminum crossover alloy is an interesting candidate for manufacturing highly loaded structures by waDED, for example, for future structures used in the aviation industry. The alloy shows robust processability and good mechanical properties. Future works should aim at optimizing processing conditions during waDED and the subsequent heat treatment.

ACKNOWLEDGEMENTS

AUTHOR CONTRIBUTIONS

TK (Conceptualization; Data curation; Formal analysis; Investigation; Methodology; Resources; Visualization; Writing—original draft); AA (Data curation; Investigation; Methodology; Writing—review & editing); MG (Data curation; Formal analysis; Investigation; Methodology; Resources; Visualization; Writing—review & editing); PB-V (Data curation; Formal analysis; Investigation; Methodology; Visualization; Writing—review & editing).

FUNDING

DATA AVAILABILITY

The data underlying this study cannot be shared at this time as they form part of an ongoing study.

CONFLICT OF INTEREST

The authors declare that they have no known conflicts of interest that could have appeared to influence the work reported in this paper.

OPEN ACCESS

REFERENCES

1. T. DebRoy, H.L. Wei, J.S. Zuback, T. Mukherjee, J.W. Elmer, J.O. Milewski, A.M. Beese, A. Wilson-Heid, A. De, and W. Zhang, *Prog. Mater. Sci.* 92, 112 (2018).
2. D. Herzog, V. Seyda, E. Wycisk, and C. Emmelmann, *Acta Mater.* 117, 371 (2016).
3. N. Mclean, M.J. Bermingham, P. Colegrove, A. Sales, and M.S. Dargusch, *Sci. Technol. Weld. Join.* 27, 479 (2022).
4. M.J. Benoit, S.D. Sun, M. Brandt, and M.A. Easton, *J. Manuf. Process.* 64, 1484 (2021).
5. D.G.E. Suyitno, and L. Katgerman, *Prog. Mater. Sci.* 49, 629 (2004).
6. T.A. Rodrigues, V. Duarte, R.M. Miranda, T.G. Santos, and J.P. Oliveira, *Materials (Basel)* 12, 1121 (2019).
7. K. Treutler, and V. Wesling, *Appl. Sci.* 11, 8619 (2021).
8. G. Venturini, F. Montevecchi, F. Bandini, A. Scippa, and G. Campatelli, *Addit. Manuf.* 22, 643 (2018).
9. T. Lehmann, D. Rose, E. Ranjbar, M. Gasri-Khouzani, M. Tavakoli, H. Henein, T. Wolfe, and A.J. Qureshi, *Int. Mater. Rev.* 67, 410 (2022).
10. H. Lockett, J. Ding, S. Williams, and F. Martina, *J. Eng. Des.* 28, 568 (2017).
11. M. Silmbroth, N. Enzinger, C. Schneider-Bröskamp, A. Arnoldt, and T. Klein, *Sci. Technol. Weld. Join.* 28, 586 (2022).
12. G. Langelandsvik, O.M. Akselsen, T. Furu, and H.J. Roven, *Materials (Basel)* 14, 1 (2021).
13. D. Oropeza, D.C. Hofmann, K. Williams, S. Firdosy, P. Bordeenithikasem, M. Sokoluk, M. Liese, J. Liu, and X. Li, *J. Alloys Compd.* 834, 154987 (2020).
14. T. Klein, A. Arnoldt, R. Lahnsteiner, and M. Schnall, *Mater. Sci. Eng. A* 830, 142318 (2022).
15. T. Klein, L. Reiter, and M. Schnall, *Mater. Lett.* 313, 131841 (2022).
16. M. Sokoluk, C. Cao, S. Pan, and X. Li, *Nat. Commun.* 10, 98 (2019).
17. T. Klein, M. Schnall, B. Gomes, P. Warczok, D. Fleischhacker, and P.J. Morais, *Addit. Manuf.* 37, 101663 (2021).
18. G. Graf, P. Spoerk-Erdely, P. Staron, A. Stark, F.M. Martin, H. Clemens, and T. Klein, *Acta Mater.* 227, 117727 (2022).
19. C. Cao, D. Zhang, L. Zhuang, and J. Zhang, *J. Alloys Compd.* 691, 40 (2017).
20. L. Stemper, M.A. Tunes, R. Tosone, P.J. Uggowitzer, and S. Pogatscher, *Prog. Mater. Sci.* 124, 100873 (2022).
21. L. Stemper, B. Mitas, T. Kremmer, S. Otterbach, P.J. Uggowitzer, and S. Pogatscher, *Mater. Des.* 181, 107927 (2019).
22. L. Stemper, M.A. Tunes, P. Oberhauser, P.J. Uggowitzer, and S. Pogatscher, *Acta Mater.* 195, 541 (2020).
23. Y. Wang, X. Wu, L. Cao, X. Tong, Y. Zou, Q. Zhu, S. Tang, H. Song, and M. Guo, *Mater. Sci. Eng. A* 804, 140515 (2021).
24. M. Köhler, S. Fiebig, J. Hensel, and K. Dilger, *Metals (Basel).* 9, 608 (2019).
25. A.G. Ortega, L.C. Galvan, M. Salem, K. Moussaoui, S. Segonds, S. Rouquette, and F. Deschaux-Beaume, *Sci. Technol. Weld. Join.* 24, 538 (2019).

26. S. Cadiou, M. Courtois, M. Carin, W. Berckmans, and P. Lemasson, *Addit. Manuf.* 36, 101541 (2020).
27. L. Yuan, Z. Pan, D. Ding, F. He, S. van Duin, H. Li, and W. Li, *Robot. Comput. Integr. Manuf.* 63, 101916 (2020).
28. T. Klein, G. Graf, P. Staron, A. Stark, H. Clemens, and P. Spoerk-Erdely, *Mater. Lett.* 303, 130500 (2021).
29. S. Kou, *Acta Mater.* 88, 366 (2015).
30. J. Liu, and S. Kou, *Acta Mater.* 125, 513 (2017).
31. E.M. Ryan, T.J. Sabin, J.F. Watts, and M.J. Whiting, *J. Mater. Process. Technol.* 262, 577 (2018).
32. M. Gudeljevic, and T. Klein, *Int. J. Adv. Manuf. Technol.* 116, 2021 (2021).
33. A. Dinsdale, C. Fang, Z. Que, and Z. Fan, *JOM* 71, 1731 (2019).
34. M. de Haas, and J.T.M. de Hosson, *Scr. Mater.* 44, 281 (2001).
35. B. Dong, X. Cai, S. Lin, X. Li, C. Fan, C. Yang, and H. Sun, *Addit. Manuf.* 36, 101447 (2020).
36. D.H. StJohn, M. Qian, M.A. Easton, and P. Cao, *Acta Mater.* 59, 4907 (2011).
37. M. Bermingham, D. StJohn, M. Easton, L. Yuan, and M. Dargusch, *JOM* 72, 1065 (2020).
38. J.A. Österreicher, G. Kirov, S.S.A. Gerstl, E. Mukeli, F. Grabner, and M. Kumar, *J. Alloys Compd.* 740, 167 (2018).
39. Z. Qi, B. Qi, B. Cong, H. Sun, G. Zhao, and J. Ding, *J. Manuf. Process.* 40, 27 (2019).
40. R. Snell, S. Tammas-Williams, L. Chechik, A. Lyle, E. Hernández-Nava, C. Boig, G. Panoutsos, and I. Todd, *JOM* 72, 101 (2020).